Analysis of Fiber Formation during Air-Gap Wet Spinning

Volker Simon
Fachgebiet Technische Strömungslehre, Technische Hochschule Darmstadt, 64287 Darmstadt, Germany

The steady formation of fibers in the air-gap wet-spinning process is analyzed, in which solidification of the fiber material is brought about by the diffusional exchange of solvent and nonsolvent in a coagulation bath. The concentration profile within the fiber is determined, and a simple model is given for the change of the material behavior with changing concentration. The material behavior of the uncoagulated spinning solution is described by a constitutive model for viscoelastic liquids that allows the incorporation of a relaxation-time spectrum. The behavior of the solidified fiber is described by a model for rubberlike elastic solids. The effects of variable fiber temperature and skin friction on the fiber motion are also taken into account. The computed velocity profiles are compared to experimental data. These data were obtained by spinning three samples of nominally identical spinning solutions. Even though the theoretically predicted profiles agree well with those obtained with the first two samples, they completely fail to do so for the third. This failure is attributed to the unexpected extreme sensitivity of the model predictions to the width of the dynamic spectrum that is used to infer the relaxation-time spectrum. It is also found that the velocity profile depends rather strongly on the initial conditions for the stress.

Introduction

Air-gap wet-spinning is a commercially important technique for producing synthetic fibers. In this process, the spinning solution is extruded through a spinneret hole as a hot liquid. The fiber is then drawn through an air gap before it is led through the coagulation bath. Finally, the fiber is collected on a windup roll at a rate that exceeds the extrusion velocity. The air gap is included in order to allow sufficient stretching of the fiber before solidification. Also, the fibers are cooled while they are traveling through the air gap. The process is shown schematically in Figure 1.

The solidification of the material is caused by a change of composition. The spinning solution is a ternary system that is composed of cellulose, solvent, and nonsolvent; the nonsolvent is usually water. In the coagulation bath, solvent diffuses out of the fiber into the bath, and water diffuses from the bath into the fiber. Because the material properties change with changing concentration, the spinning solution coagulates and a solidified outer skin is formed that resists further deformation. Simple dynamic shear flow measurements of the uncoagulated hot spinning solution reveal its viscoelastic liquidlike behavior. Likewise, dynamic elongational flow measurements of the solidified fiber indicate a viscoelastic solidlike behavior of the freshly spun wet fiber. Experiments also show that the viscosity of the spinning solution strongly depends on temperature.

There is an ever-increasing demand to improve the quality of the fibers as well as to increase their production rate. The fiber quality depends, of course, on composition, molecular structure, and on the specific kinds of cellulose and solvent that are used. More important, however, is the deformation history, that is, the rate of stretching prior to coagulation. Stretching creates a high degree of orientation of the molecules, and this imparts the strength to the material. The rate of stretching also affects the production rate of the fibers and therefore determines whether or not a production line is economical and efficient. Stretching, cooling, and coagulation are processes that occur concurrently and that influence each other. In order to optimize the fiber quality as well as their production rate, one has to consider all of these processes and their interactions.

Present address: Siemens AG, 45466 Mülheim a.d. Ruhr, Germany.

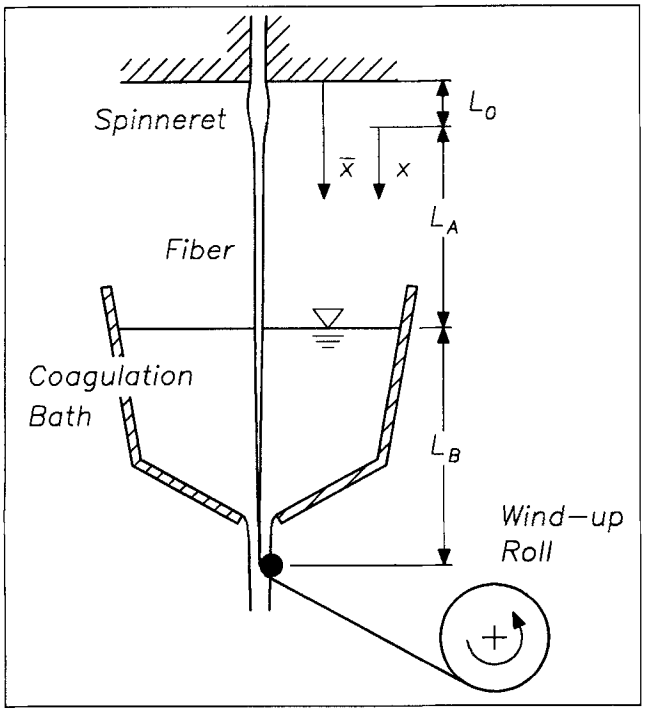

Figure 1. Spinning process.

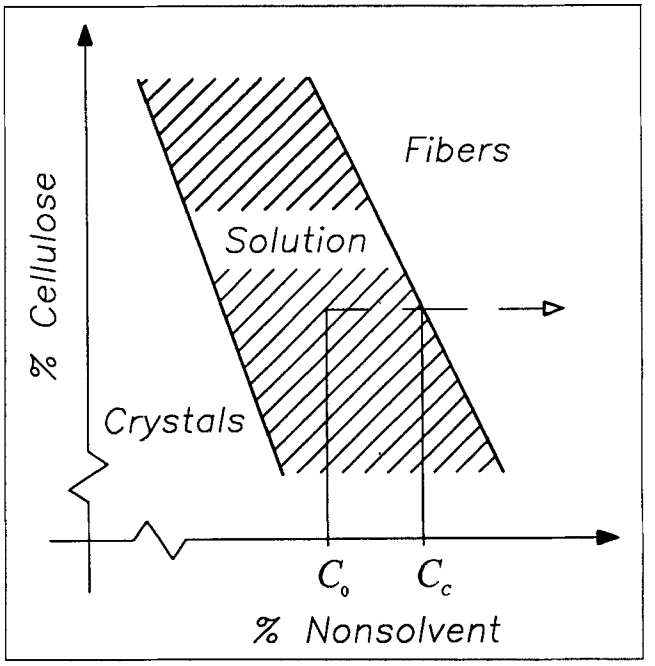

Figure 2. Solubility diagram.

– – – →: change of state during wet-spinning.

It is the purpose of this article to provide such an analysis of fiber formation, taking into account the transfer of heat and mass and the corresponding change of the material behavior. Only then are we in a position to draw comparisons with experiments and to scrutinize the model. Even though there exists a substantial literature on the mechanics of melt-spinning (see, e.g., the reviews by Denn (1980), Denn (1983), Mewis and Petrie (1987) and the monograph by Petrie (1979)), comparatively few analyses have been devoted to the analysis of wet-spinning. The only treatment of the air-gap wet-spinning process that we are aware of has recently been given by Simon (1992), and the current article is essentially an extension of this work. In the previous analyses of wet-spinning, such as those by White and Hancock (1981), Han and Segal (1970), Han (1976), and Ziabicki (1976), the fiber has always been assumed to be a Newtonian material exhibiting a concentration-dependent viscosity. Obviously, this assumption is inadequate to model the observed material behavior in the present case.

In this article, the liquid-solid phase transition is modeled by assuming that coagulation occurs instantaneously once the solvent concentration drops below a critical value. Further changes of the material behavior with changing composition in the liquid and the solid phases are ignored. This is justified because the ratio of the shear modulus of the solidified fiber to the mean shear modulus of the uncoagulated spinning solution is rather large. The critical value of concentration at which fully coagulated material is observed can be read off a solubility diagram such as that shown in Figure 2. The position in the fiber at which the concentration attains this critical value may then be obtained after we have determined the concentration distribution in the fiber. Instantaneous solidification at a given value of concentration implies a sharp boundary separating the liquid and the solid parts of the fiber and different rheological behavior in these phases. The liquid uncoagulated spinning solution is assumed to behave like a viscoelastic Phan-Thien fluid (Phan-Thien, 1978), and the solid coagulated material is assumed to behave like a nonlinear elastic solid. Our model of the solidification process is similar to the one advanced by Cao and Campbell (1990), who modeled the solidification during film blowing. The model of a two-phase fiber also resembles the problem of bicomponent spinning as analyzed by Park (1990). In contrast to bicomponent spinning, however, material particles cross the phase boundary in the current application, whereas in bicomponent spinning material particles move along the interface.

The outline of the article is as follows. We first provide the equations of motion for slender fiber flows along with the relevant initial and boundary conditions. These equations are usually simplified by assuming that the axial velocity as well as the axial and radial stress components are constant over any cross section of the fiber (Matovich and Pearson, 1969; Denn et al., 1975). Here, we carry this idea further and assume that the axial velocity is not only constant over a cross section, but also that it is the same for core and skin layers. Likewise, the axial and radial stress components, although different in the liquid and the solid part of the fiber, are assumed to be constant over the respective cross sections. The flow in and near the spinneret is, however, intrinsically two-dimensional and is therefore excluded in the present analysis. Consequently, the origin of the coordinate system is placed at a position somewhat below the point of maximum die swell (Figure 1). After we have presented the equations that govern the fiber motion, we describe the determination of skin friction, fiber temperature, and concentration profile in the fiber.

Finally, we compare the predicted velocity profiles to experimental data. The agreement is satisfactory in most cases. In some cases, however, the model predictions fail to reproduce the experimental data. The cause of this failure is investigated, and it is found that the model predictions are extremely sensitive to the shape of the relaxation-time spectrum and the width of the dynamic spectrum that are used to calculate it. Specifically, the data at low shearing frequencies contain important information about the material behavior. If this information is available, the model predictions are fairly good; if this information is missing, the predictions are useless. We also find a rather strong dependence of the velocity profile on the initial conditions for the stress.

Equations of Motion

We restrict our analysis to steady, axisymmetric fiber flow and write all equations with respect to a cylindrical coordinate system that has its origin placed somewhat below the spinneret. The mass flux of the fiber is constant in the spinning process, hence $\dot{V} = \pi u_F a^2 = \text{const}$. We assume that the axial fiber velocity u_F is a function of x only. Then, the radial velocity component $v_F = -r/2 \cdot du_F/dx$. Neglecting inertia, gravity, and surface tension, an integral momentum balance for the fiber in the bath yields

$$0 = 2\pi \frac{d}{dx}\left(\int_0^{a_c} \tau_{xx}^L \, r dr\right) + 2\pi \frac{d}{dx}\left(\int_{a_c}^{a} \tau_{xx}^S \, r dr\right) + \frac{dF}{dx}, \quad (1)$$

where

$$dF = -\pi \tau_{xx}^S(a)\, da^2 + 2\pi a \tau_{rx}^S(a)\, dx \quad (2)$$

is the x-component of the force acting on the fiber surface. We insert Eq. 2 into Eq. 1, use the relation $\boldsymbol{\tau} = -p\boldsymbol{I} + \boldsymbol{P}$ between the stress tensor $\boldsymbol{\tau}$, pressure p, and the tensor of the extra stresses $\boldsymbol{P}$, and assume that P_{xx}^L, P_{rr}^L, p^L, and P_{xx}^S, P_{rr}^S, p^S depend on x only. This yields

$$0 = \frac{d}{dx}[(P_{xx}^L - p^L)a_c^2] + \frac{d}{dx}[(P_{xx}^S - p^S)(a^2 - a_c^2)] - \tau_{xx}^S \frac{da^2}{dx} + 2a\tau_{rx}^S(a). \quad (3)$$

Here, superscripts L and S denote quantities in the liquid and the solid part of the fiber, and a_c denotes the radius that separates these phases. At the fiber surface $r = a(x)$ and at the phase interface $r = a_c(x)$, and the stress boundary conditions are, respectively,

$$\boldsymbol{n} \cdot (\boldsymbol{\tau}^S - \boldsymbol{\tau}^E) = 0 \quad \text{at} \quad r = a(x), \quad (4)$$

and

$$\boldsymbol{n}_c \cdot (\boldsymbol{\tau}^L - \boldsymbol{\tau}^S) = 0 \quad \text{at} \quad r = a_c(x). \quad (5)$$

The unit normal vectors $\boldsymbol{n}$ and $\boldsymbol{n}_c$ are given by

$$\boldsymbol{n} = (\boldsymbol{e}_r - a'\boldsymbol{e}_x)/[1 + (a')^2]^{1/2} \quad \text{and}$$

$$\boldsymbol{n}_c = (\boldsymbol{e}_r - a_c'\boldsymbol{e}_x)/\left[1 + (a_c')^2\right]^{1/2}, \quad (6)$$

where a prime denotes differentiation with respect to x and the superscript E refers to quantities in the environment of the fiber. The pressure p^E on the outer surface of the fiber is approximately equal to the ambient pressure p_0 along the entire fiber surface. All components of $\boldsymbol{P}^E$ may be neglected when compared to $\boldsymbol{P}^S$, except the shear stress $\tau_{rx}^E \equiv \tau_w$ that is exerted on the fiber due to its motion through the bath.

Over most of the spinline the radii a and a_c are slowly varying quantities with $a' \sim a/L$ and $a_c' \sim a/L$. These estimates hold except at the point where the fiber dives into the bath. This point represents a singularity, and both a and a_c will change rapidly in its neighborhood. Nevertheless, we will ignore terms multiplied by $(a')^2$ and $(a_c')^2$ in Eqs. 4 and 5. This approximation will be good everywhere except in the immediate vicinity of this singular point. Then, decomposing Eq. 4 into its axial and radial components yields

$$\tau_{rx}^S = \tau_w + a'(\tau_{xx}^S + p_0) \quad \text{at} \quad r = a(x), \quad (7)$$

and

$$\tau_{rr}^S = -p_0 \quad \text{or} \quad p^S = p_0 + P_{rr}^S \quad \text{at} \quad r = a(x). \quad (8)$$

Likewise, the decomposition of Eq. 5 leads to

$$\tau_{rx}^L - \tau_{rx}^S = a_c'(\tau_{xx}^L - \tau_{xx}^S) \quad \text{at} \quad r = a_c(x), \quad (9)$$

and

$$\tau_{rr}^S = \tau_{rr}^L \quad \text{or} \quad p^L = p_0 + P_{rr}^L \quad \text{at} \quad r = a_c(x). \quad (10)$$

Upon inserting Eqs. 7, 8, and 10 into Eq. 3 we obtain

$$0 = \frac{d}{dx}[(P_{xx}^L - P_{rr}^L)a_c^2] + \frac{d}{dx}[(P_{xx}^S - P_{rr}^S)(a^2 - a_c^2)] + 2a\tau_w(x). \quad (11)$$

This equation is applicable to the fiber motion in the bath. In the air gap, we may neglect the shear stress τ_w and put $a_c = a$. Then, the equation reduces to

$$0 = \frac{d}{dx}[(P_{xx}^L - P_{rr}^L)a^2] \quad \text{or} \quad (P_{xx}^L - P_{rr}^L)\pi a^2 = F_0 = \text{const}. \quad (12)$$

In order to progress, we need to specify the material behavior in the liquid and the solid phases. The viscoelastic liquid spinning solution is described by the constitutive model proposed by Phan-Thien (1978). This model allows for a spectrum of relaxation times and decomposes the tensor of extra stresses $\boldsymbol{P}^L$ into N spectral modes $\boldsymbol{P}_{(i)}^L$ according to

$$\boldsymbol{P}^L = \sum_{i=1}^{N} \boldsymbol{P}^L_{(i)}. \tag{13}$$

The stresses $\boldsymbol{P}^L_{(i)}$ are related to the tensors $\boldsymbol{E} = 1/2(\nabla\boldsymbol{u} + \nabla\boldsymbol{u}^T)$ and $\boldsymbol{\Omega} = 1/2(\nabla\boldsymbol{u} - \nabla\boldsymbol{u}^T)$ by

$$K_i\boldsymbol{P}_{(i)} + \lambda_i\phi(T)\frac{D^*_{(\xi)}}{Dt}\boldsymbol{P}_{(i)} = 2G_i\lambda_i\phi(T)\boldsymbol{E}, \tag{14}$$

where

$$K_i = \exp\left[\frac{\epsilon}{G_i}\,\mathrm{tr}\,(\boldsymbol{P}_{(i)})\right] \quad \text{and} \quad \phi(T) = \exp\left[\frac{E}{RT_R}\left(\frac{T_R}{T} - 1\right)\right], \tag{15}$$

and the general time derivative is given by

$$\frac{D^*_{(\xi)}}{Dt}\boldsymbol{P}^L_{(i)} = \frac{D}{Dt}\boldsymbol{P}^L_{(i)} + \boldsymbol{\Omega}\cdot\boldsymbol{P}^L_{(i)} - \boldsymbol{P}^L_{(i)}\cdot\boldsymbol{\Omega} + \xi\left(\boldsymbol{P}^L_{(i)}\cdot\boldsymbol{E} + \boldsymbol{E}\cdot\boldsymbol{P}^L_{(i)}\right). \tag{16}$$

We note that the solution viscosity strongly depends on temperature through the function $\phi(T)$. In addition to the relaxation spectrum, characterized by the relaxation times λ_i and the corresponding shear moduli G_i, the model contains two material parameters, ξ and ϵ. These parameters can be determined in simple shear and elongational flow measurements, respectively.

The solid part of the fiber is assumed to behave like a rubberlike, nonlinear elastic solid with modulus G_S, and its viscoelastic features are neglected:

$$\frac{D^*_{(\xi=1)}}{Dt}\boldsymbol{P}^S = 2G_S\boldsymbol{E}. \tag{17}$$

Along the spinline, the kinematic tenors $\boldsymbol{E}$ and $\boldsymbol{\Omega}$ take the form

$$\boldsymbol{E} \simeq \frac{1}{2}\frac{du_F}{dx}\begin{bmatrix} -1 & 0 & 0 \\ 0 & -1 & 0 \\ 0 & 0 & 2 \end{bmatrix} \quad \text{and} \quad \boldsymbol{\Omega} \simeq 0, \tag{18}$$

where we have neglected terms of order a/L and used the fact that $u_F = u_F(x)$. Upon inserting Eq. 18 into Eqs. 14 and 17, we find that the components $P_{\varphi\varphi}$ and P_{rr} satisfy the same differential equation. If we assume that the initial values of these stresses are the same, they remain the same throughout the entire deformation path.

The equations that describe the evolution of the stress and velocity fields in the fiber in the bath are easily obtained from Eqs. 11 and 14 to 18:

$$\frac{du_F}{dx} = \frac{A_1 + A_2 + A_3}{A_4 + A_5}, \tag{19}$$

$$\frac{d}{dx}P^L_{xx(i)} = \frac{2}{u_F}\frac{du_F}{dx}\left(G_i + \xi P^L_{xx(i)}\right) - \frac{K_iP^L_{xx(i)}}{\lambda_i\phi(T)u_F}, \tag{20}$$

$$\frac{d}{dx}P^L_{rr(i)} = -\frac{1}{u_F}\frac{du_F}{dx}\left(G_i + \xi P^L_{rr(i)}\right) - \frac{K_iP^L_{rr(i)}}{\lambda_i\phi(T)u_F}, \tag{21}$$

$$\frac{d}{dx}P^S_{xx} = \frac{2}{u_F}\frac{du_F}{dx}(G_S + P^S_{xx}), \tag{22}$$

$$\frac{d}{dx}P^S_{rr} = -\frac{1}{u_F}\frac{du_F}{dx}(G_S + P^S_{rr}), \tag{23}$$

and

$$K_i = \exp\left[\frac{\epsilon}{G_i}(P^L_{xx} + 2P^L_{rr})\right], \tag{24}$$

where we have used the abbreviations

$$A_1 = \delta^2\sum_{i=7}^{N}\left\{K_i\left(P^L_{xx(i)} - P^L_{rr(i)}\right)/[\lambda_i\phi(T)]\right\}, \tag{25}$$

$$A_2 = 2\delta\frac{d\delta}{dx}u_F(P^S_{xx} - P^S_{rr} - P^L_{xx} + P^L_{rr}), \tag{26}$$

$$A_3 = -2\pi a u_F^2\tau_w(x)/\dot{V}, \tag{27}$$

$$A_4 = \delta^2\left[3\sum_{i=1}^{N}G_i + P^L_{xx}(2\xi - 1) + P^L_{rr}(\xi + 1)\right], \tag{28}$$

$$A_5 = (1 - \delta^2)(3G_S + P^S_{xx} + 2P^S_{rr}), \tag{29}$$

and

$$\delta = a_c(x)/a(x). \tag{30}$$

In the air gap, $\tau_w \approx 0$ and $\delta = 1$. Then, Eqs. 22 and 23 are obsolete, the coefficients $A_2 = A_3 = A_5 = 0$, and the remaining equations reduce to those commonly employed for melt spinning calculations.

Initial and Boundary Conditions

The preceding equations have to be supplemented by initial and boundary conditions. Spinning is a two-point boundary value problem, where it is assumed that the initial and takeup velocities are known:

$$u_F = u_0 \quad \text{at} \quad x = 0, \tag{31}$$

and

$$u_F = u_E \quad \text{at} \quad x = L_A + L_B. \tag{32}$$

Instead of prescribing the take-up velocity, we can specify the axial force that acts upon the fiber in the air gap:

$$(P^L_{xx} - P^L_{rr})\pi a^2 = F_0 \quad \text{at} \quad x = 0, \tag{33}$$

or the force that is applied to draw the fiber:

$$(P_{xx}^S - P_{rr}^S)\pi(a^2 - a_c^2) + (P_{xx}^L - P_{rr}^L)\pi a_c^2 = F_L \quad \text{at} \quad x = L_A + L_B. \quad (34)$$

If the material were Newtonian, the conditions 31 and 32 (or 31 and 33 or 34) would suffice to assure the well-posedness of the problem. Due to its elasticity, however, the state of the material also depends upon the deformation history. Using a differential constitutive model, the information about prior deformation must be supplied through initial values for some of the stress components. Using a single relaxation time, $N = 1$, it is sufficient to prescribe $P_{xx}^L(x = 0)$. The value of $P_{rr}^L(x = 0)$ is then given by Eq. 12. Using a spectrum of N relaxation times, $2N - 1$ initial values for the stress components have to be specified. Denn and Marrucci (1977) proposed that the ratios $P_{rr(i)}^L(x = 0)/P_{xx(i)}^L(x = 0)$ and $P_{xx(i)}^L(x = 0)/P_{xx(N)}^L(x = 0)$ be assigned those values that they would attain in fully developed pipe flow. This seems to be a reasonable choice, because the deformation history is dominated by the tubelike flow through the spinneret. For fully developed pipe flow we obtain from Eq. 14, with $\epsilon = 0$ and $\xi = 1$:

$$\frac{P_{rr(i)}^L}{P_{xx(i)}^L} = 0 \quad \text{and} \quad \frac{P_{xx(i)}^L}{P_{xx(N)}^L} = \frac{\lambda_i^2 G_i}{\lambda_N^2 G_N} \quad \text{at} \quad x = 0. \quad (35)$$

In contrast, Phan-Thien (1978) suggested an even distribution of the stresses over the different modes:

$$\frac{P_{rr(i)}^L}{P_{xx(i)}^L} = 0 \quad \text{and} \quad \frac{P_{xx(i)}^L}{P_{xx(N)}^L} = 1 \quad \text{at} \quad x = 0. \quad (36)$$

Although both distributions are merely assumptions about the state of the fluid at some point in the flow, we expect that the conditions in Eq. 35 are the more realistic ones, because they make an attempt to reflect the prior deformation.

Modeling isothermal melt-spinning of LDPE, Denn et al. (1975) and Phan-Thien (1978) both note that their computed velocity profiles are insensitive to the specific initial conditions for the stress that they use. In order to investigate the sensitivity of our model to the initial stress conditions, we will compare profiles that are based on the distributions in Eqs. 35 and 36 in the results section.

The sudden change of the material behavior due to coagulation also necessitates prescription of initial stress conditions along the phase boundary $r = a_c(x)$. Nothing is known about these conditions and, so far, the problem has not been addressed in the literature. Here, we set

$$P_{xx}^S = P_{xx}^L \quad \text{and} \quad P_{rr}^S = P_{rr}^L \quad \text{at} \quad x = L_A, \quad (37)$$

and the assumption of constant cross-sectional stresses in the solid phase implies that these stresses are imposed along the phase boundary by the already solidified part of the fiber.

The numerical computation is most conveniently carried out using dimensionless quantities. The selection of an appropriate measure of nondimensional distance is guided by the observation that $\tau_w \sim (x - L_A)^{-1/2}$ (see the next section). Therefore, we choose

$$\zeta_A = \frac{x}{L_A + L_B} \quad \text{if} \quad x \le L_A, \quad (38)$$

and

$$\zeta_B = \sqrt{\zeta_A - L_A/(L_A + L_B)} \quad \text{if} \quad x \ge L_A. \quad (39)$$

The dimensionless velocity and stresses are given by

$$U = \frac{u_F}{u_0}, \quad S_i^L = P_{rr(i)}^L \frac{\dot{V}}{F_0 u_0}, \quad T_i^L = P_{xx(i)}^L \frac{\dot{V}}{F_0 u_0}, \quad (40)$$

$$S^S = P_{rr}^S \frac{\dot{V}}{F_0 u_0}, \quad \text{and} \quad T^S = P_{xx}^S \frac{\dot{V}}{F_0 u_0}. \quad (41)$$

This leads to the following dimensionless products that govern the fiber motion in the spinning process:

$$Dr = \frac{u_E}{u_0}, \quad De_0 = \frac{\lambda_0 u_0}{L_A + L_B}, \quad \chi = \frac{G_0 \dot{V}}{F_0 u_0}, \quad (42)$$

$$\gamma = \frac{G_S}{G_0}, \quad \alpha_i = \frac{G_i}{G_0}, \quad \beta_i = \frac{\lambda_i}{\lambda_0}, \quad (43)$$

$$W_1 = \frac{\rho_B u_0^2}{G_0}, \quad W_2 = \frac{\nu_B (L_A + L_B)}{u_F a^2}, \quad \text{and} \quad c_f = 2\frac{\tau_w}{\rho_B u_F^2}, \quad (44)$$

where ρ_B and ν_B are the density and kinematic viscosity of the liquid in the bath, and the mean values are defined as

$$\lambda_0 = \sum_{i=1}^{N} \lambda_i^2 G_i / \sum_{i=1}^{N} \lambda_i G_i, \quad \eta_0 = \sum_{i=1}^{N} \lambda_i G_i, \quad \text{and} \quad G_0 = \eta_0/\lambda_0. \quad (45)$$

The resulting set of equations is most easily solved as an initial-value problem with prescribed initial velocity ($U = 1$ at $\zeta_A = 0$) and a guessed value of the axial force χ; the draw ratio $Dr = U(\zeta_A = 1)$ is then obtained as part of the solution. By varying χ, we can obtain any value of Dr that we wish.

Before we proceed and solve the equations of fiber motion, however, we have to determine

- The coefficient of skin friction c_f, as it appears in Eqs. 19 through 44
- The fiber temperature, as it influences the solution viscosity through the function $\phi(T)$ (cf. Eq. 15)
- The concentration distribution in the fiber, and from this the phase interface $\delta = a_c/a$.

Skin Friction

In the bath, the moving fiber produces an axisymmetric, laminar boundary layer in which the fluid velocity decays from

its value $u_F(x_B)$ at the fiber surface to zero at large distances. Here, we have set $x_B = x - L_A$. There is some fluid motion in the bath even if the fiber were at rest. This motion is due to the efflux of fluid through the orifice at the bottom of the bath and to the fillup of fluid at the top. However, this background flow is very small as compared to the motion that is induced by the movement of the fiber. Consequently, we will neglect this background flow and treat the flow as being that which is produced by a fiber moving through a fluid at rest. In the surroundings of the fiber, the pressure gradient due to gravity is negligible, hence $p^E = p_0 = \text{const}$, and all physical properties are taken to be constant. Then the balance equations of continuity and momentum are given by (Sakiadis, 1961):

$$\frac{\partial}{\partial x_B}(ru) + \frac{\partial}{\partial r}(rv) = 0 \tag{46}$$

and

$$u\frac{\partial u}{\partial x_B} + v\frac{\partial u}{\partial r} = \frac{\nu_B}{r}\frac{\partial}{\partial r}\left(r\frac{\partial u}{\partial r}\right). \tag{47}$$

Sakiadis (1961) applied a Pohlhausen method to solve Eqs. 46 and 47 and determined the skin friction accordingly. Crane (1972) solved the equations by means of series expansions. These expansions are valid close to the beginning of the boundary layer development and far downstream but lack an intermediate region of common validity. Therefore, we solved the equations numerically, using the numerical scheme proposed by Herring and Mellor (1970). In doing so, we follow Crane (1972) and adopt the dimensionless axial coordinate

$$X = \sqrt{\frac{8\nu_B x_B}{u_F a^2}}. \tag{48}$$

The numerical solution of Eqs. 46 and 47 then yields the coefficient of skin friction c_f as a function of X:

$$c_f\sqrt{\frac{u_F(x_B)x_B}{\nu_B}} = \text{fn}(X). \tag{49}$$

Münzing (1992) found that the coefficient of skin friction for a fiber moving with a linearly increasing velocity $u_F(x_B)$ differs by at most 8% from the one determined with $u_F = \text{const}$. Therefore, we set $u_F = \text{const}$ for the determination of skin friction in our application.

Fiber Temperature in the Air Gap

It is necessary to obtain knowledge about the fiber temperature in the spinning process because the solution viscosity depends on temperature (cf. Eq. 15). Several analyses treat the problem of convective fiber cooling as the fiber moves through a fluid that is otherwise at rest. The results of these analyses, however, fail to reproduce the experimentally determined fiber temperature in the air gap: the predicted values for the fiber temperature are higher than those measured in the experiments. The reason for this failure is that in air-gap wet-spinning the fibers contain water; the water evaporates at the fiber surface, and this contributes to the cooling of the fiber. Here, we only give a brief synopsis of fiber cooling in the air gap; a detailed analysis is given elsewhere (Simon, 1994).

The cooling mechanism is as follows. The saturation concentration of water vapor at the fiber surface is fixed by the condition of thermodynamic equilibrium and depends on ambient pressure, water content within the fiber, and fiber temperature. At the spinneret, the fiber temperature is rather high, and the corresponding value of concentration of water vapor at the fiber surface exceeds the value of concentration of water vapor in the ambient air. As a result, a concentration gradient is established, and this leads to a mass flux of water vapor that is directed from the fiber to the surrounding air. This mass flux is maintained by continuous evaporation of water at the fiber surface, and the heat necessary for evaporation is withdrawn from the fiber. This leads to a more rapid cooling in this process as compared to melt spinning.

Evaporation and convection lead to a decrease of fiber temperature with increasing distance from the spinneret. With decreasing temperature, however, the concentration of water vapor at the fiber surface also decreases and eventually falls below the value in the ambient air. Then, the mass flux of water vapor is directed from the environment to the fiber, and water vapor condenses at the fiber surface. The heat that is released by condensation is then delivered to the fiber. The ultimate fiber temperature exceeds the temperature in the surrounding air and is determined by the equilibrium between heat removal by convection and heat supply by condensation.

Simon (1994) has shown that the temperature is approximately constant over a cross section of the fiber and that the concentration does not change within the fiber in the air gap. In this case, an appropriate measure of distance from the spinneret is

$$X_A = \sqrt{\frac{8\nu_A \bar{x}}{u_F a^2}}. \tag{50}$$

The fiber temperature T_F in the air gap must be obtained numerically as a function of X_A:

$$\Theta_{F,A} = \frac{T_F - T_{A,\infty}}{T_{F,0} - T_{A,\infty}} = \text{fn}(X_A), \tag{51}$$

where $T_{F,0}$ denotes the initial fiber temperature and $T_{A,\infty}$ denotes the temperature of the ambient air.

Fiber Temperature in the Coagulation Bath

In the bath, the temperature fields in the fiber and its surroundings are functions of radial as well as of axial position. We take all physical properties to be constant and neglect axial relative to radial heat conduction. Then, the governing equations are

$$u_F \frac{\partial T_F}{\partial x} + v_F \frac{\partial T_F}{\partial r} = \frac{\kappa_F}{r} \frac{\partial}{\partial r}\left(r \frac{\partial T_F}{\partial r}\right) \quad \text{if} \quad r \le a(x), \quad (52)$$

and

$$u \frac{\partial T_B}{\partial x} + v \frac{\partial T_B}{\partial r} = \frac{\kappa_B}{r} \frac{\partial}{\partial r}\left(r \frac{\partial T_B}{\partial r}\right) \quad \text{if} \quad r \ge a(x), \quad (53)$$

where T_B is the temperature in the bath. These equations have to satisfy the initial and boundary conditions

$$T_F = T_F(L_A) \quad \text{at} \quad x = L_A \quad r < a(x), \quad (54)$$

$$T_B = T_{B,\infty} \quad \text{at} \quad x = L_A \quad r > a(x), \quad (55)$$

$$T_B \to T_{B,\infty} \quad \text{at} \quad x \ge L_A \quad r \to \infty, \quad (56)$$

$$\frac{\partial T_F}{\partial r} = 0 \quad \text{at} \quad x \ge L_A \quad r = 0, \quad (57)$$

and

$$T_F = T_B, \quad \lambda_F \frac{\partial T_F}{\partial r} = \lambda_B \frac{\partial T_B}{\partial r} \quad \text{at} \quad x \ge L_A \quad r = a(x). \quad (58)$$

In these equations, $T_F(L_A)$ is the fiber temperature at the end of the air gap, and $T_{B,\infty}$ is the ambient temperature in the bath. In general, the velocity components $u(x, r)$ and $v(x, r)$ in Eq. 53 have to be determined by solving the relevant equations of motion of the fluid in the bath.

Depending on the value of the Prandtl number $Pr = \nu/\kappa$, however, the temperature boundary layer will be smaller ($Pr > 1$) or larger ($Pr < 1$) than the velocity boundary layer, and this will aid in simplifying the problem (see, e.g., Griffith (1964) and Spurk (1993)). If, for example, $Pr \gg 1$, as is the case in our application, the temperature boundary layer is much smaller than the velocity boundary layer and the temperature variation is confined to a layer in which the velocity of the fluid is approximately equal to the fiber velocity. It is therefore permissible to replace $u(x, r)$ by $u_F(x)$ and $v(x, r)$ by $v_F(x, r)$ in Eq. 53. Here, we have $Pr \approx 7$, and we will assume that this value is large enough to justify this simplification. If we furthermore introduce the variables

$$\eta = \frac{r}{a(x)}, \quad \xi_T = \frac{\kappa_F (x - L_A)}{u_F(x) a^2(x)}, \quad \text{and}$$

$$\Theta_{F,B} = \frac{T_F - T_{B,\infty}}{T_F(L_A) - T_{B,\infty}}, \quad (59)$$

then neither the variable fiber velocity nor the changing fiber radius appears in the differential equations or in the initial and boundary conditions. Consequently, the fiber temperature in the bath $\Theta_{F,B}(\eta, \xi_T)$ is independent of the specific functional form of $u_F(x)$ or $a(x)$. The equations that result by applying the transformation 59 also describe the time-dependent temperature field in an infinite cylinder of constant diameter. This problem was treated by Carslaw and Jaeger (1959), who found the solution to be

$$\Theta_{F,B} = \frac{4\Re_2}{\pi^2} \int_0^\infty \exp(-\xi_T s^2) \frac{J_0(s\eta) J_1(s)}{s^2(\phi^2(s) + \psi^2(s))} ds, \quad (60)$$

where

$$\phi(s) = J_1(s) Y_0(\Re_1 s) - \Re_1 \Re_2 J_0(s) Y_1(\Re_1 s),$$

$$\psi(s) = J_1(s) J_0(\Re_1 s) - \Re_1 \Re_2 J_0(s) J_1(\Re_1 s) \quad (61)$$

with

$$\Re_1 = \sqrt{\kappa_F/\kappa_B} \quad \text{and} \quad \Re_2 = \lambda_B/\lambda_F. \quad (62)$$

$J_i(s)$ and $Y_i(s)$ are Bessel functions of the ith order of first and second kind, respectively. The mean fiber temperature is given by

$$\overline{\Theta}_{F,B}(\xi_T) = 2 \int_0^1 \Theta_{F,B}(\eta, \xi_T) \eta \, d\eta$$

$$= \frac{8\Re_2}{\pi^2} \int_0^\infty \exp(-\xi_T s^2) \frac{(J_1(s))^2}{s^3(\phi^2(s) + \psi^2(s))} ds. \quad (63)$$

In our application, $\Re_1 = 0.514$ and $\Re_2 = 5.66$.

Concentration Distribution and Phase Interface

As was pointed out in the introduction, the spinning solution is assumed to coagulate and solidify instantaneously when the solvent concentration drops below a critical value. In order to find the position at which the concentration attains this critical value we have to determine the concentration distribution within the fiber in the bath. This is done in this section.

It is known from laboratory experiments that a batch of spinning solution preserves its volume when solvent diffuses out and water diffuses into it. Also, the densities of solvent and water are nearly the same. This implies that the diffusional mass fluxes of solvent and water have the same magnitude but opposite direction at the fiber surface. As a consequence, the density as well as the mass flux of the fiber are conserved in the spinning process.

The cellulose acts much like a matrix that is not involved in the diffusion process. Therefore, an appropriate and convenient measure of concentration is the mass fractions w_n and w_s of water and solvent, respectively, where $w_n + w_s = 1$ (Paul, 1968). Even though the diffusion coefficient D for the binary mixture of solvent and water depends on temperature, this dependence is neglected, because this allows an analytic solution to be obtained.

As stated earlier, the concentration in the fiber is unaltered by the evaporation of the water in the air gap. Therefore, the concentration at the beginning of the bath is given by the value w_{n0} with which the fiber left the spinneret. Finally, we neglect axial as compared to radial diffusion.

With the preceding assumptions, the governing equations as well as the initial and boundary conditions that describe

the concentration distribution are obtained from Eqs. 52 to 58 if we replace $(T_F, T_B, T_A(L_A), T_{B,\infty}, \kappa, \lambda)$ by $(w_n, w_n, w_{n0}, w_{n\infty}, D, 1)$, respectively. The role that was formerly played by the Prandtl number is now taken on by the Schmidt number $Sc = \nu/D$. For liquids, $Sc \approx 10^4$, so that we can again replace $u(x, r)$ by $u_F(x)$ and $v(x, r)$ by $v_F(x, r)$. The solution to the diffusion equations is then given by Eqs. 60 to 62 if we set $\Re_1 = \Re_2 = 1$ and replace $\Theta_{F,B}$ and ξ_T by

$$C = \frac{w_n - w_{n\infty}}{w_{n0} - w_{n\infty}} \quad \text{and} \quad \xi_D = \frac{D(x - L_A)}{u_F(x)a^2(x)}, \tag{64}$$

respectively. This yields a relation of the form $C = \text{fn}(r/a, \xi_D)$. The phase interface is now given by those values of $\delta = a_c/a$ and ξ_D for which the concentration C attains its critical value C_c. Therefore, we have to invert the relation $C_c = \text{fn}(\delta = a/a_c, \xi_D)$ to yield $\delta = \text{fn}(C_c, \xi_D)$. This has to be done numerically, but even then it is cumbersome to carry out.

A much simpler and more instructive solution is obtained by exploiting the fact that the thickness of the concentration boundary layer $\sqrt{D(x - L_A)/u_F}$ in the fiber is much smaller than the fiber radius a. Typically, $DL_B/(u_F a^2) \approx 10^{-4}$ in the spinning process. Therefore, the concentration profile in the fiber is unaffected by the fiber radius. This suggests a change of variables according to

$$\xi_D = \sqrt{\frac{4D(x - L_A)}{u_F a^2}} \quad \text{and} \quad \eta_D = \frac{r - a}{a}\sqrt{\frac{u_F a^2}{4D(x - L_A)}}. \tag{65}$$

Inserting Eq. 65 into the differential equation and letting $\xi_D \to 0$ yields

$$C'' = -2\eta_D C', \tag{66}$$

where a prime denotes differentiation with respect to η_D. The solution to Eq. 66 that satisfies the boundary conditions

$$C \to 0 \quad \text{at} \quad \eta_D \to \infty \quad \text{and} \quad C \to 1 \quad \text{at} \quad \eta_D \to -\infty \tag{67}$$

is

$$C = \frac{1}{2}[1 - \text{erf}(\eta_D)]. \tag{68}$$

This solution allows the explicit determination of δ as a function of C_c and axial position, because a constant value of C_c requires a constant value of η_D, hence

$$\delta = 1 + \text{const}\sqrt{\frac{4D(x - L_A)}{u_F a^2}}. \tag{69}$$

In all our applications, the value of the critical concentration as obtained from the solubility diagram is $C_c = 0.95$. This yields const $= -1.16$. The approximate solution Eq. 69 differs by at most 4% from the numerically determined solution, provided $D(x - L_A)/(u_F a^2)$ is smaller than 4×10^{-4}. We note that for typical spinning conditions, $\delta \approx 0.8$ at the end of the bath.

Results and Discussion

Our solution strategy is as follows. Equations 19–21 and 19–23 constitute two systems of $2N + 1$ and $2N + 3$ first-order ordinary differential equations that describe the fiber motion in the air gap and in the bath, respectively. These systems were solved numerically as initial-value problems with prescribed initial velocity and a guessed value of the axial force. The applied winding force was then adjusted until a given velocity at some point downstream was attained. If not stated otherwise, we have used the initial conditions for the stress as proposed by Denn and Marrucci (1977), Eq. 35.

The coefficient of skin friction c_f, the fiber temperature in the air gap $\Theta_{F,A} = (T_F - T_{A,\infty})/(T_{F,0} - T_{A,\infty})$, and the fiber temperature in the bath $\bar{\Theta}_{F,B} = (T_F - T_{B,\infty})/[T_F(L_A) - T_{B,\infty}]$ were determined numerically using the techniques described earlier. The position of the phase interface δ is calculated using Eq. 69. The values of c_f, $\Theta_{F,A}$, and $\bar{\Theta}_{F,B}$ are tabulated as functions of X, X_A, and ξ_T, respectively. The relations between these coordinates and the coordinates ζ_A and ζ_B that are used to solve the equations of fiber motion are

$$X = \sqrt{8W_2}\,\zeta_B, \qquad X_A = \sqrt{8W_3[\zeta_A + L_0/(L_A + L_B)]}, \tag{70}$$

$$\xi_T = W_4\zeta_B^2, \quad \text{and} \quad \xi_D = 2\sqrt{W_5}\,\zeta_B, \tag{71}$$

where

$$W_2 = \frac{\nu_B(L_A + L_B)}{u_F a^2}, \qquad W_3 = \frac{\nu_A(L_A + L_B)}{u_F a^2}, \tag{72}$$

$$W_4 = \frac{\kappa_F(L_A + L_B)}{u_F a^2}, \quad \text{and} \quad W_5 = \frac{D(L_A + L_B)}{u_F a^2}. \tag{73}$$

The dependence of viscosity on temperature is reflected by the function (cf. Eq. 15)

$$\phi(\Theta_{F,A}) = \exp\left[\frac{W_7(W_6 - \Theta_{F,A})}{\Theta_{F,A} + W_8}\right] \tag{74}$$

and the parameters

$$W_6 = \frac{T_R - T_{A,\infty}}{T_{F,0} - T_{A,\infty}}, \quad W_7 = \frac{E}{RT_R} \quad \text{and} \quad W_8 = \frac{T_{A,\infty}}{T_{F,0} - T_{A,\infty}}. \tag{75}$$

The fiber temperatures $\Theta_{F,A}$ and $\bar{\Theta}_{F,B}$ are related through

$$\Theta_{F,A} = \bar{\Theta}_{F,B}W_9 - W_{10}, \tag{76}$$

where

$$W_9 = \frac{T_F(L_A) - T_{B,\infty}}{T_{F,0} - T_{A,\infty}} = \Theta_{F,A}(x = L_A) + W_{10}$$

$$\text{and} \quad W_{10} = \frac{T_{A,\infty} - T_{B,\infty}}{T_{F,0} - T_{B,\infty}}. \quad (77)$$

The additional dimensionless parameters that control the fiber temperature in the air gap are given by Simon (1994).

Before calculating the results, it is necessary to assign suitable values to the parameters $W_1, \ldots, W_{10}$. In the analysis of the preceding sections, these parameters were regarded as constants, but through the physical properties ν, κ, and D some of them depend on temperature. We have chosen to evaluate ν, κ, and D at a mean temperature $T_m = (T_0 - T_\infty)/2$.

The material parameter ξ was determined by fitting the shear viscosity to experimentally determined dynamic shear moduli via the Cox-Merz rule; this yields $\xi = 0.9$ in all our applications. No data on pure elongational flow were available. Therefore, we have put $\epsilon = 0.015$ throughout. From numerical experiments, however, we found that the results are not very sensitive to the values of ϵ or ξ. The value of ϵ may even be changed by as much as 50% without changing the velocity profile appreciably. However, ϵ may not be set to zero: in this case, the constitutive model degenerates to the upper-convected-Maxwell model (UCMM). As Denn and Marrucci (1977) have shown, the UCMM does not permit solutions if $De_0(Dr - 1) \geq 1$. In our application, $De_0(Dr - 1) \geq 1$ for all experimental setups investigated. It is therefore vital to have a small but nonvanishing value of ϵ.

We note that the Deborah number $De_0 = u_0\lambda_0/(L_A + L_B)$ and the function $\phi(\Theta_{F,A})$ always appear together in the governing equations, whence we put $De \equiv De_0\phi(\Theta_{F,A})$. Due to the temperature dependence of the relaxation time λ_0, De_0 refers to the reference temperature at which λ_0 and η_0 were measured, while De refers to the actual temperature in the process. Typical spinning conditions are characterized by draw ratios Dr ranging between 6 and 24 and Deborah numbers De ranging between 1 and 10. We found that within these ranges the minimum number of relaxation times that have to be incorporated is $N \approx 10$. This is in contrast to the findings of Denn and Marrucci (1977), who found that only three to four modes are necessary when modeling the spinning of LDPE with a UCMM. We attribute our different finding to the fact that we are dealing with a cellulosic spinning solution whose rheological behavior (i.e., the relaxation spectrum) is very different from that of LDPE. All subsequent computations were carried out using $N = 12$ relaxation modes.

We now compare the theoretically predicted fiber velocities to experimentally determined ones. The experiments have been carried out using three samples of nominally identical spinning solutions. These samples are denoted by A, B, and C. The relaxation time spectra of these samples were computed from dynamic storage and loss moduli $G'(\omega)$ and $G''(\omega)$ ($\omega \equiv$ shearing frequency) by the maximum entropy method (Gull and Skilling, 1984; Elster and Honerkamp, 1991). The computed spectra are shown in Figure 3.

Note that the spectra for samples A and B are nearly indistinguishable except for small relaxation times, while the spectrum of sample C deviates substantially from the other two. This is surprising because all three samples are derived from nominally identical spinning solutions, and we would expect all three spectra to coincide. A possible reason for this deviation is discussed later in this section. We anticipate, however, that the deviations in the spectra will manifest themselves in deviations between model predictions and experiments.

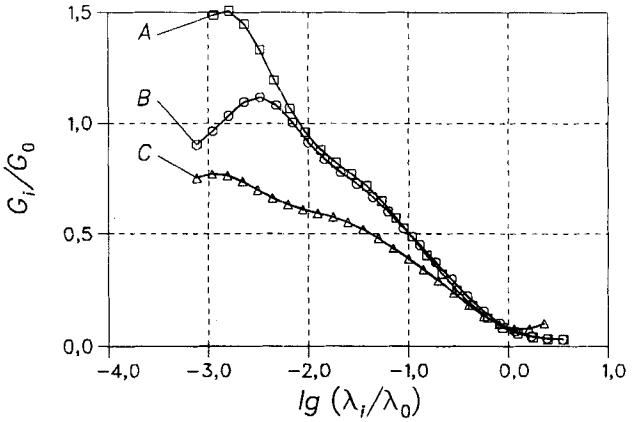

Figure 3. Relaxation spectra $\{G_i, \lambda_i\}$ for samples *A*, *B*, and *C*.

These samples are derived from nominally identical spinning solutions.

The experimentally determined velocity profiles were obtained in six experimental setups, denoted by I to VI. The setups I, II, and III were carried out using spinning solution of sample A; setup IV was carried out using spinning solution of sample B; and setups V and VI were carried out using spinning solution of sample C. The setups differed in volume flow rate, initial and take-up velocities, in the parameter W_7, and in the relaxation-time spectra, depending on which sample had been used; all other parameters were the same. The dimensionless parameters are shown in Table 1. Also tabulated are the computed values of the axial tension χ. Unfortunately, neither F_0 nor F_L could be measured in the

Table 1. Parameters for Experimental Setups I to VI

Setup	I	II	III	IV	V	VI
Dr	4.01	8.18	22.67	24.00	18.33	23.89
De_0	1.44	3.34	1.16	2.09	1.03	1.14
De	4.57	5.84	7.36	5.19	4.89	1.71
$\chi \times 10^2$	3.62	2.34	1.91	2.10	3.53	3.46
$G_S/G_0 \times 10^{-3}$	5.40	5.40	5.40	4.90	156.70	93.10
$\dot{V}/\dot{V}_1$	1.00	2.79	0.35	1.47	0.90	1.34
$W_1 \times 10^2$	4.44	23.84	2.90	6.39	4.39	5.37
W_2	115.30	41.37	327.30	78.55	128.50	86.22
$W_3 \times 10^{-3}$	1.80	0.64	5.10	1.22	2.00	1.34
W_4	16.50	5.92	46.81	11.23	18.39	12.33
$W_5 \times 10^3$	6.69	2.40	18.98	4.56	7.46	5.00
W_6	0.94	0.94	0.94	0.94	0.94	0.94
W_7	14.64	14.64	14.64	19.95	6.11	6.11
W_8	3.97	3.97	3.97	3.97	3.97	3.97
$W_9 \times 10$	6.75	8.49	4.92	7.44	6.55	7.27
W_{10}	0.14	0.14	0.14	0.14	0.14	0.14

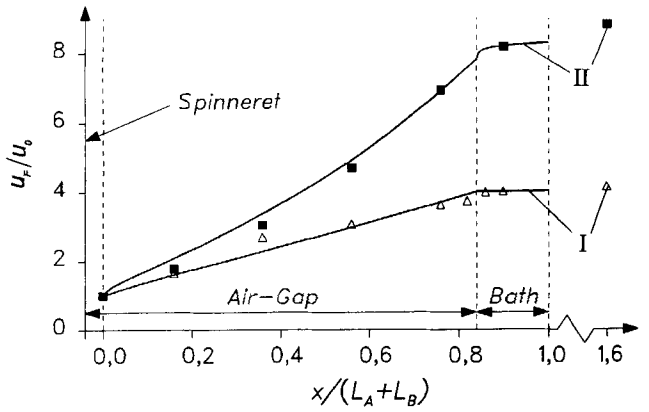

Figure 4. Measured (symbols) and predicted (solid lines) fiber velocity, setups I and II.

Both setups were carried out using spinning solution of sample *A*.

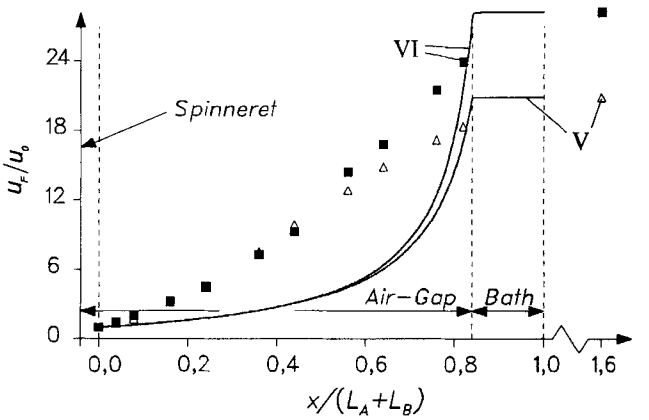

Figure 6. Measured (symbols) and predicted (solid lines) fiber velocity, setups V and VI.

Both setups were carried out using spinning solution of sample *C*.

experiments. The computed and experimental velocity profiles are compared in Figures 4, 5, and 6. Even though the agreement is satisfactory in those cases in which spinning dope of samples *A* and *B* was used, the theory appears to fail completely for those cases that were obtained with sample *C*.

To investigate this failure, we first inspect the values of the nondimensional parameters that the calculations are based upon. As can be seen from Table 1, the parameters that underlie the calculations for setups III to VI are all of the same order of magnitude; these setups differ mainly in the spectra that were used in the calculations and in the parameter W_7. This suggests we recalculate setups V and VI using the spectrum of sample *A* instead of that of *C*. This has been done and the results are shown in Figures 7 and 8. Now, the agreement is rather satisfactory. Also shown in Figures 7 and 8 are profiles calculated with the spectrum of sample *A* and the corresponding different value of W_7. Obviously, the failure to reproduce setups V and VI is not due to a faulty theory but to the special kind of spectrum that is used. We may now ask: What causes the spectrum of sample *C* to differ so much from the other two spectra?

A possible cause for the deviation would, of course, be inaccurate measurements of the data that underlie the spectrum. As is well known, the spectrum $\{G_i, \lambda_i\}$ cannot be measured in an experiment directly. Rather, one subjects a batch of the spinning solution to oscillatory shearing with frequency ω and measures the dynamic moduli $G'(\omega)$ and $G''(\omega)$. Yet both the experimental method of determining G' and G'' as well as the method that is used to convert the data G' and G'' into the spectrum $\{G_i, \lambda_i\}$ are very reliable and accurate. This accuracy is sustained by the fact that the measured data G' and G'' of samples *A*, *B*, and *C* do not differ noticeably. However, it is not known in advance nor is it in any way obvious over which frequency range G' and G'' have to be measured.

In order to examine the influence of the frequency range on the relaxation-time spectrum we consider five different spectra $\{G_i, \lambda_i\}$ denoted by *a* to *e*. These spectra are based

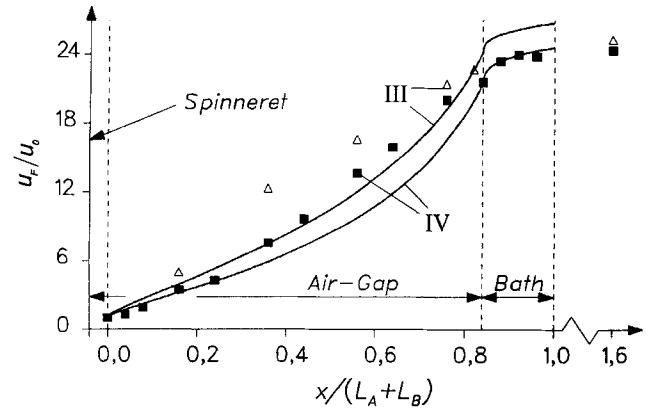

Figure 5. Measured (symbols) and predicted (solid lines) fiber velocity, setups III and IV.

Setup III was carried out using spinning solution of sample *A*; setup IV was carried out using spinning solution of sample *B*.

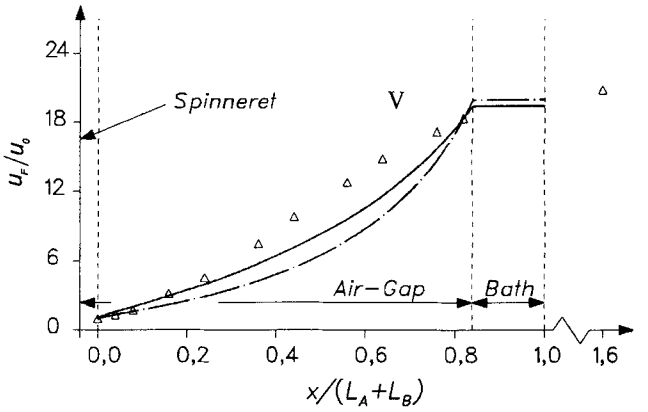

Figure 7. Measured (symbols) and predicted (solid lines) fiber velocity for setup V.

The calculations are based on the spectrum of sample *A*. The solid line denotes a calculation with $W_7 = 14.1$; the chain-dotted line designates a calculation with $W_7 = 6.1$.

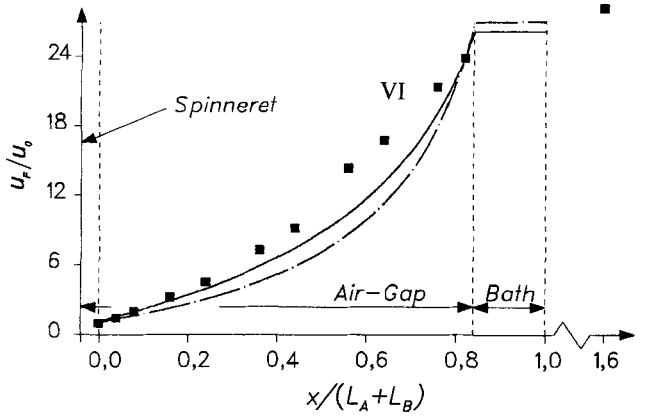

Figure 8. Measured (symbols) and predicted (solid lines) fiber velocity for setup VI.

The calculations are based on the spectrum of sample *A*. The solid line denotes a calculation with $W_7 = 14.1$; the chain-dotted line designates a calculation with $W_7 = 6.1$.

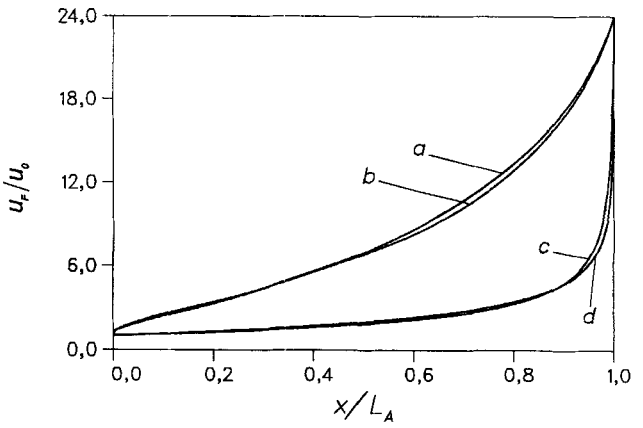

Figure 10. Calculated isothermal velocity profiles in the air gap with Deborah number *De* = 10 and draw ratio *Dr* = 24, for the truncated spectra *a*, *b*, *c*, and *d*.

on the dynamic data G', G'' obtained from sample *A*. Spectrum *a* was determined using all available dynamic data; spectrum *b* was determined by discarding one-third of the available data at the high frequency range; spectrum *c* was determined by discarding one-third of the data at the high and low frequency ranges; spectrum *d* was determined by discarding one-third of the data at the low frequency range; and spectrum *e* was determined by discarding one-third of the data at an intermediate frequency range. The widths of the different spectra are sketched in Figure 9. The calculations based on spectrum *e* were almost indistinguishable from those based on spectrum *a*. We therefore conclude that the spectral data at intermediate frequencies are insignificant and ignore spectrum *e* in the remainder of this section.

Depending on the different amount of information contained within the spectra *a* to *d*, each of them has a different mean relaxation time and a different mean shear modulus. These mean values are collected in Table 2. If we were to compare our calculations to experimental data, the initial velocity and the length of the spinline would be set by the experimenter. Using the mean relaxation times as calculated for the four different spectra, we would arrive at different values for the Deborah number, depending on the spectrum we would use. To render the results comparable, we assign the Deborah number *De* values of 10.0, 10.0, 2.66, and 1.34 for the spectra *a*, *b*, *c*, and *d*, respectively. With these, we have computed isothermal velocity profiles in the air gap. The results are shown in Figure 10.

This figure reveals that those spectra that are based on data truncated at the low frequency end lead to false velocity profiles. In particular, these profiles exhibit a strong positive curvature, as was the case with setups V and VI. Obviously, the information about the material behavior that is contained in the low frequency end of the dynamic data G' and G'' is most important. This importance may be explained by noting that data at low frequencies will most strongly affect the largest relaxation times. These, in turn, will dominate the flow (see, e.g., Petrie (1978) and Petrie (1979)). This result confirms our earlier supposition that the failure of correctly predicting the experimental velocities for setups V and VI is caused by the particular form of spectrum *C*. It is conceivable that the experimental data at low frequencies are less accurate than those at higher frequencies or that the measurements were simply not carried out at low enough frequencies.

Even though it would be desirable to extend the measurements of the dynamic data in the low frequency range and repeat the calculations, there are two reasons for not doing

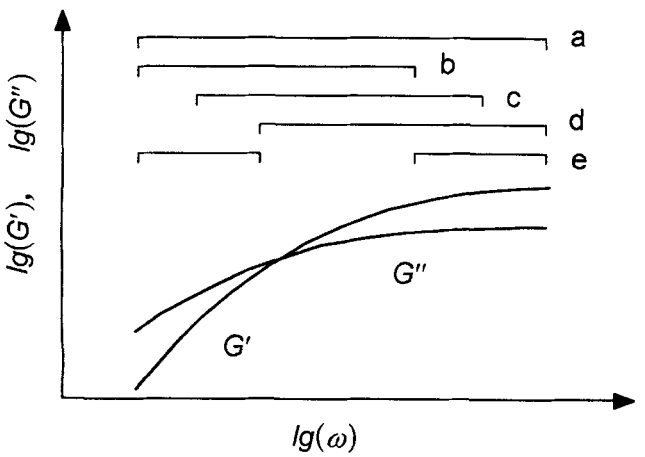

Figure 9. Dynamic moduli G′ (ω) and G″(ω) vs. shearing frequency ω (qualitatively) and different widths used to infer $\{G_i, \lambda_i\}$ for the spectra *a* to *e*.

Table 2. Mean Relaxation Time, Shear Modulus, and Viscosity for the Truncated Spectra *a* to *d*

	$\lambda_0/\lambda_{0,a}$	$G_0/G_{0,a}$	$\eta_0/\eta_{0,a}$
a	1.00	1.00	1.00
b	0.96	1.02	0.99
c	0.27	2.74	0.73
d	0.13	4.13	0.55

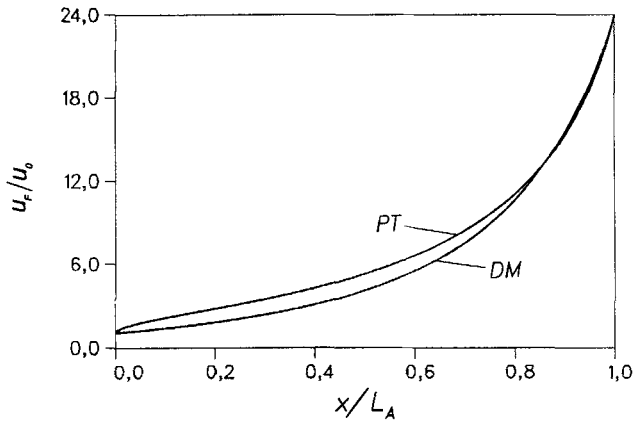

Figure 11. Calculated isothermal velocity profiles in the air gap for Deborah number *De* = 1 and draw ratio *Dr* = 24 for different initial stress conditions.

Calculations that are based on the initial stress conditions proposed by Phan-Thien (1978) are designated by *PT*; calculations that are based on the initial stress conditions proposed by Denn and Marrucci (1977) are designated by *DM*.

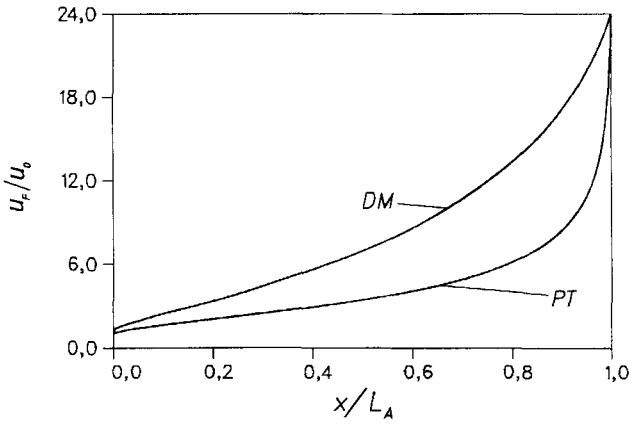

Figure 12. Calculated isothermal velocity profiles in the air gap for Deborah number *De* = 10 and draw ratio *Dr* = 24 for different initial stress conditions.

Calculations that are based on the initial stress conditions proposed by Phan-Thien (1978) are designed by *PT*; calculations that are based on the initial stress conditions proposed by Denn and Marrucci (1977) are designated by *DM*.

this: first, the measurements have already been carried to the low frequency limit at which commercial viscometers can be operated, taking into account the viscosity-temperature shift; and second, at low frequencies the time that is necessary to gather the experimental data may be so large that an appreciable amount of the water that is contained within the fiber evaporates, thus altering the material behavior. This last reason may have also influenced the poor quality of the measurements at the low frequency range.

Honerkamp (1989) has shown how adding small bits of information or knowledge about the asymptotic behavior of the spectrum (for $\lambda \to 0$ or for $\lambda \to \infty$) can substantially improve the quality of the final spectrum. It is thus advisable to measure the equilibrium viscosity η_0 independent of the dynamic measurements. Equation 45 can then be imposed as a further constraint on the determination of G_i and λ_i.

We now turn to the question of which initial conditions for the stress should be chosen. In their simulations of isothermal spinning of LDPE, Denn et al. (1975) and Phan-Thien (1978) found only a weak dependence of the velocity profiles on the initial stress conditions. In order to assure ourselves whether or not this weak dependence prevails in the current case we have calculated isothermal velocity profiles in the air gap for the Deborah number and draw ratio ranges of interest, using both the initial stress conditions proposed by Denn and Marrucci (1977) and those proposed by Phan-Thien (1978). The results are depicted in Figure 11 for $De = 1$ and $Dr = 24$, and in Figure 12 for $De = 10$ and $Dr = 24$. It is quite interesting to learn that for a low Deborah number the curvature of the profiles based upon the conditions of Denn and Marrucci is larger than the curvature based on the conditions of Phan-Thien, while for a larger Deborah number this effect is reversed. This remarkable sensitivity to the initial stress conditions is in contrast to the results of Denn et al. (1975) and Phan-Thien (1978), and we attribute it to the specific spectrum that was used, that is, to the use of a material different from LDPE.

Of course, the true initial conditions must be determined by calculating the two-dimensional flow through the spinneret. As long as this information is missing, we favor the initial conditions of Denn and Marrucci, which seem to be the more realistic ones.

In concluding this section we display the calculated stresses for setups I and IV in the Figures 13 and 14, respectively. It is interesting to note that for setup I, the normal stress difference in the liquid part of the fiber continuously decreases in the bath, while for setup IV, the same normal stress difference increases with increasing distance in the bath. For a Newtonian fluid, the stresses would diminish as the rate of deformation goes to zero. When spinning a fluid that exhibits elasticity, the development of the stresses is not as obvious. We would, however, expect some residual stresses to persist.

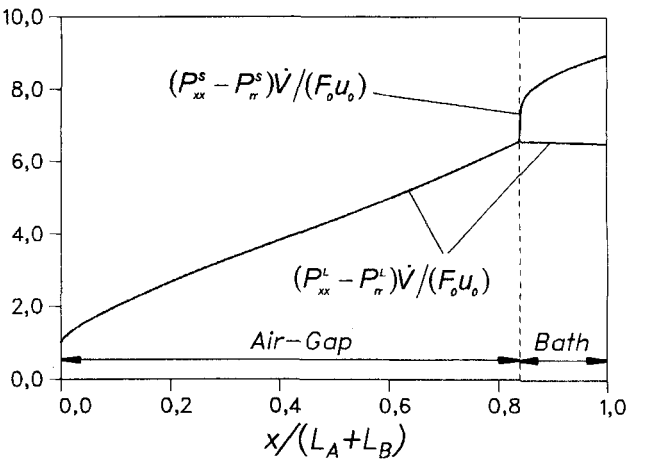

Figure 13. Calculated normal stress differences in the liquid and solid parts of the fiber for setup I.

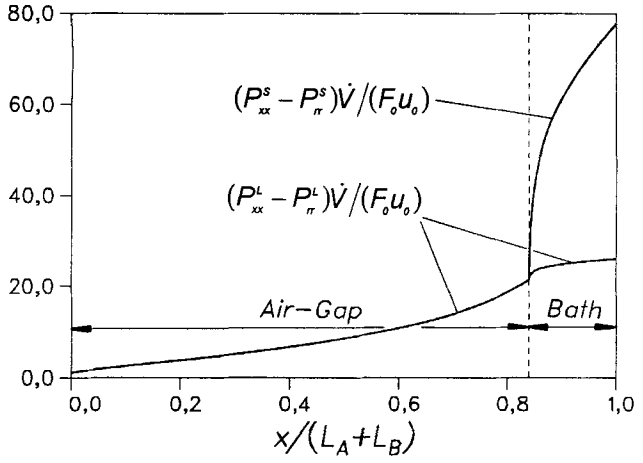

Figure 14. Calculated normal stress differences in the liquid and solid parts of the fiber for setup IV.

Conclusions

We have introduced a new and simple model that describes the formation of fibers in the air gap wet-spinning process. The model takes into account the viscoelastic liquidlike behavior of the uncoagulated spinning solution, the elastic solidlike behavior of the coagulated material, and the change of the material behavior with changing concentration. The temperature dependence of the solution viscosity as well as the skin friction acting on the surface of the fiber in the bath are also taken into account.

The computed velocity profiles are compared to experimental data. Even though the theoretically predicted velocity profiles agree well with the experimental data in most cases, they fail to reproduce others. This failure is shown to be caused by the special relaxation time spectrum that is used in the calculation. This spectrum is incomplete in the sense that it does not contain all the necessary information about the material behavior. In particular, we found that the information that is contained in the low frequency range of the dynamic spectrum is of paramount importance and is missing in some of the cases considered.

From the results of the previous section we conclude that, in order to make quantitatively correct predictions, it is necessary to:

- Take into account the temperature dependence of the solution viscosity and, consequently, to determine the temperature variation along the spinline
- Allow for a viscoelastic behavior of the spinning solution
- Incorporate approximately $N = 10$ spectral modes
- Use the initial stress conditions proposed by Denn and Marrucci (1977) in a one-dimensional approach
- Measure the dynamic data, especially in the low frequency limit.

The constitutive equations that model the behavior of the coagulated spinning solution appear to be too simplistic. A more realistic constitutive model for the coagulated fiber should allow for viscoplastic–elastic flow and some degree of strain hardening. A model of this type has been proposed by Cao and Campbell (1990). Unfortunately, however, this model appears to lack a sound theoretical and experimental basis. Also, it is extremely difficult to measure all relevant material properties in the regime where the solid-liquid phase transition occurs.

We feel that our approach gives reasonably good results with input data that are easily accessible and measurable in any actual process.

Acknowledgments

All experimental data were provided by Akzo Research Laboratories, Obernburg. This work was initiated by Professor J. H. Spurk, to whom I am deeply indebted for his advice and helpful discussions. I am also grateful to Dr. G. Frischmann for valuable and stimulating conversations. Last but not least I thank Professor J. T. Jenkins for critically reading the manuscript.

Notation

E = activation energy
F = axial tension
K_i = function, defined in Eq. 15
L = axial length
L_0 = distance between spinneret and origin of coordinate system
R = gas constant
S, S_i = dimensionless radial stress component, defined as $S_i = P_{rr(i)}\dot{V}/(F_0 u_0)$
T, T_i = dimensionless axial stress component, defined as $T_i = P_{xx(i)}\dot{V}/(F_0 u_0)$
u_0, u_E = initial and take-up velocity, respectively
U = dimensionless fiber velocity, defined as $U = u_F/u_0$
$\dot{V}$ = volume flow rate, defined as $\dot{V} = \pi u_F a^2$
W_i = dimensionless parameters, defined in Eqs. 44, 72, 73, 75 and 77
x, r = axial and radial coordinate, respectively

Greek letters

α_i = ratio of shear moduli, defined as $\alpha_i = G_i/G_0$
β_i = ratio of relaxation times, defined as $\beta_i = \lambda_i/\lambda_0$
γ = parameter, defined as $\gamma = G_S/G_0$
η_0 = zero-shear viscosity
η, η_D = dimensionless radial coordinates, defined in Eqs. 59 and 65, respectively
ξ_D, ξ_T = dimensionless axial coordinates, defined in Eqs. 63 and 59, respectively
$\mathbf{\Omega}$ = spin tensor, defined as $\Omega = (\nabla\vec{u} - \nabla\vec{u}^T)/2$
$\Re_1, \Re_2$ = parameters, defined as $\Re_1 = \sqrt{\kappa_F/\kappa_B}$ and $\Re_2 = \lambda_B/\lambda_F$

Subscripts and Superscripts

n = nonsolvent (water)
$(i), i$ = ith relaxation mode
R = reference state
0 = at origin of the coordinate system
∞ = at infinity
T = transpose

Literature Cited

Cao, B., and G. A. Campbell, "Viscoplastic-Elastic Modeling of Tubular Blown Film Processing," *AIChE J.*, **36**, 420 (1990).
Carslaw, H. S., and J. C. Jaeger, *Conduction of Heat in Solids*, 2nd ed., Oxford Univ. Press, London (1959).
Crane, L. J., "Boundary Layer Flow on a Circular Cylinder Moving in a Fluid at Rest," *Z. Angew. Math. Phys.*, **23**, 201 (1972).
Denn, M. M., C. J. S. Petrie, and P. Avenas, "Mechanics of Steady Spinning of a Viscoelastic Liquid," *AIChE J.*, **21**, 791 (1975).
Denn, M. M., and G. Marrucci, "Effect of a Relaxation Time Spec-

trum on Mechanics of Polymer Melt Spinning," *J. Non-Newtonian Fluid Mech.*, **2**, 159 (1977).
Denn, M. M., "Continuous Drawing of Liquids to Form Fibers," *Annu. Rev. Fluid Mech.*, **12**, 365 (1980).
Denn, M. M., "Fiber Spinning," *Computational Analysis of Polymer-Processing*, J. R. A. Pearson and S. M. Richardson, eds., Applied Science, London/New York, p. 179 (1983).
Elster, C., and J. Honerkamp, "A Modified Maximum Entropy Method and Its Application to Creep Data," *Macromol.*, **24**, 310 (1991).
Griffith, R. M., "Velocity, Temperature, and Concentration Distribution During Fibre Spinning," *Ind. Eng. Chem. Fundam.*, **3**, 245 (1964).
Gull, S. F., and J. Skilling, "Maximum Entropy Method in Image Processing," *Proc. IEEE*, **131F**, 646 (1984).
Han, C. D., and L. Segal, "A Study of Fiber Extrusion in Wet-Spinning. II. Effects of Spinning Conditions on Fiber Formation," *J. Appl. Poly. Sci.*, **14**, 2999 (1970).
Han, C. D., *Rheology in Polymer Processing*, Academic Press, New York (1976).
Herring, H. J., and G. L. Mellor, "A Computer Program to Calculate Incompressible Laminar and Turbulent Boundary Layer Development," *NACA Rep. CR1564* (1970).
Honerkamp, J., "Ill-Posed Problems in Rheology," *Rheol. Acta*, **28**, 363 (1989).
Matovich, M. A., and J. R. A. Pearson, "Spinning a Molten Threadline," *Ind. Eng. Chem. Fundam.*, **8**, 512 (1969).
Mewis, J., and C. J. S. Petrie, "Hydrodynamics of Spinning Polymers," in *Encyclopedia of Fluid Mechanics*, Gulf Publ., N. P. Cheremisinoff, ed., Houston, p. 111 (1987).
Münzing, R., "Temperaturverteilung im Spinnfaden," Diploma Thesis, Fachgebiet Technische Strömungslehre, Technische Hochschule Darmstadt, unpublished (1992).
Park, C.-W., "Extensional Flow of a Two-Phase Fiber," *AIChE J.*, **33**, 197 (1990).
Paul, D. R., "Diffusion During the Coagulation Step of Wet-Spinning," *J. Appl. Poly. Sci.*, **12**, 383 (1968).
Petrie, C. J. S., "Some Results in the Theory of Melt Spinning for Model Viscoelastic Liquids," *J. Non-Newtonian Fluid Mech.*, **4**, 137 (1978).
Petrie, C. J. S., *Elongational Flows*, Pitman, London (1979).
Phan-Thien, N., "A Nonlinear Network Viscoelastic Model," *J. Rheol.*, **22**, 259 (1978).
Sakiadis, B. C., "Boundary Layer Behaviour on Continuous Solid Surfaces: I. Boundary-Layer Equations for Two-Dimensional and Axisymmetric Flow," *AIChE J.*, **7**, 26 (1961).
Simon, V., "The Mechanics of Air-Gap Wet-Spinning of Fibers," *Theoretical and Applied Rheology, Proc. Int. Cong. Rheology, Brussels*, P. Moldenaers and R. Keunings, eds., Elsevier, Amsterdam, p. 391 (1992).
Simon, V., "The Temperature of Fibers During Air-Gap Wet-Spinning: Cooling by Convection and Evaporation," *Int. J. Heat Mass Transf.*, **37**, 1133 (1994).
Spurk, J. H., *Strömungslehre*, 3rd ed., Springer-Verlag, Berlin (1993).
White, J. L., and T. A. Hancock, "Fundamental Analysis of the Dynamics, Mass Transfer, and Coagulation in Wet-Spinning of Fibers," *J. Appl. Poly. Sci.*, **26**, 3157 (1981).
Ziabicki, A., *Fundamentals of Fibre Formation*, Wiley, London, (1976).

Manuscript received Feb. 7, 1994, and revision received May 11, 1994.